PNAS RESEARCH ARTICLE | PHYSICS

Correlated topological flat bands in rhombohedral graphite

Hongyun Zhang[a,1], Qian Li[a,1], Michael G. Scheer[b], Renqi Wang[a], Chuyi Tuo[c], Nianlong Zou[a], Wanying Chen[a], Jiaheng Li[a], Xuanxi Cai[a], Changhua Bao[a], Ming-Rui Li[c], Ke Deng[a], Kenji Watanabe[d], Takashi Taniguchi[e], Mao Ye[f], Peizhe Tang[g,h], Yong Xu[a,i], Pu Yu[a,i], Jose Avila[j], Pavel Dudin[j], Jonathan D. Denlinger[k], Hong Yao[c], Biao Lian[b], Wenhui Duan[a,c,i], and Shuyun Zhou[a,i,2]

Affiliations are included on p. 6.

Edited by Angel Rubio, Max-Planck-Institut fur Struktur und Dynamik der Materie, Hamburg, Germany; received May 29, 2024; accepted September 10, 2024

Flat bands and nontrivial topological physics are two important topics of condensed matter physics. With a unique stacking configuration analogous to the Su–Schrieffer–Heeger model, rhombohedral graphite (RG) is a potential candidate for realizing both flat bands and nontrivial topological physics. Here, we report experimental evidence of topological flat bands (TFBs) on the surface of bulk RG, which are topologically protected by bulk helical Dirac nodal lines via the bulk-boundary correspondence. Moreover, upon in situ electron doping, the surface TFBs show a splitting with exotic doping evolution, with an order-of-magnitude increase in the bandwidth of the lower split band, and pinning of the upper band near the Fermi level. These experimental observations together with Hartree–Fock calculations suggest that correlation effects are important in this system. Our results demonstrate RG as a platform for investigating the rich interplay between nontrivial band topology, correlation effects, and interaction-driven symmetry-broken states.

topological flat bands | helical Dirac nodal lines | correlated efffects | rhombohedral graphite

Significance

Searching for materials with both flat bands and nontrivial topology is fundamentally important to realize exotic physical properties. Here, we experimentally report the rhombohedral graphite as an ideal candidate with existence of surface topological flat bands, which are protected by bulk helical Dirac nodal lines. Moreover, the surface topological flat bands show correlation effects, which are evidenced by the splitting and exotic evolution upon in situ electron doping. Our results demonstrate the rhombohedral graphite as a platform for bridging the two interesting fields of nontrivial topological physics and flat-band-induced electronic instabilities.

The stacking order as well as the twisting angle of graphene layers provides a control knob for inducing flat band and emergent phenomena, such as superconductivity (1), correlated insulation (2), quantum anomalous Hall effect (3, 4), and fractional quantum anomalous Hall effect (5). In few-layer rhombohedral graphene with ABC stacking order, a wide range of intriguing properties have been reported in few-layer flakes with varying thickness as well as in moiré superstructures. For example, the bandgap and transport properties are highly tunable by an electric field (6–8). Interaction-driven correlated phenomena and competing symmetry-broken states, such as Mott insulation, superconductivity, ferromagnetism, and ferroelectricity, have been reported in trilayer flakes and moiré superlattices (9–14), tetralayer and heterostructures (15–17), and even thicker rhombohedral graphene systems (18–20). More interestingly, the quantum anomalous Hall effect (4) and the fractional quantum anomalous Hall effect (5) have been recently discovered in pentalayer rhombohedral graphene moiré heterostructures.

The origin of these interesting correlated phenomena is a band flattening effect that occurs near the K and K′ points. The bands nearest the Fermi level E_F exhibit a power law behavior, $E \approx \pm|k|^N$, where E is the electron energy, k is the two-dimensional momentum relative to the K or K′ point, and N is the number of graphene layers (21–27). As the parent compound of few-layer rhombohedral graphene, bulk rhombohedral graphite (bulk RG) is expected to have an even flatter band, which could further enhance instabilities toward interaction-driven symmetry-broken states. Moreover, its unique stacking sequence makes it a potential three-dimensional topological semimetal with $\mathbb{Z}_2$ topological charge (28), for hosting both bulk topological physics and flat band, which can go beyond the physics of twisted bilayer graphene and few-layer rhombohedral graphene. In addition, exotic properties such as topological, chiral, or high-temperature surface superconductivity (29, 30) have also been predicted. It is therefore important to investigate whether bulk RG exhibits correlation effect and nontrivial topological properties.

In this work, we report direct experimental evidence of surface topological flat bands (surface TFBs) with correlation effects in RG using angle-resolved photoemission spectroscopy (ARPES) with micrometer- or nanometer-scale beam size (MicroARPES or NanoARPES). Weakly dispersing surface TFBs are clearly observed near the K and K′ points, along with corresponding bulk helical Dirac nodal lines (DNLs). Upon in situ electron doping, the surface TFBs in the K valley split into two bands, the lower

Author contributions: S.Z. designed the research; H.Z., Q.L., W.C., C.B., X.C., K.D., M.Y., J.A., P.D., J.D., and S.Z. performed the ARPES measurements and analyzed the ARPES data; H.Z. and Q.L. prepared the samples; H.Z., Q.L., and P.Y. performed the AFM and Raman measurements; M.S., R.W., C.T., N.Z., J.L., M.L., P.T., Y.X., H.Y., B.L., and W.D. performed the calculations; K.W. and T.T. prepared BN crystals; H.Z. and S.Z. wrote the manuscript; and all authors commented on the manuscript.

The authors declare no competing interest.

This article is a PNAS Direct Submission.

[1]H.Z. and Q.L. contributed equally to this work.

[2]To whom correspondence may be addressed. Email: syzhou@mail.tsinghua.edu.cn.

This article contains supporting information online at https://www.pnas.org/lookup/suppl/doi:10.1073/pnas.2410714121/-/DCSupplemental.

Published October 16, 2024.

of which (labeled as lower band) increases in the bandwidth by an order of magnitude, while the upper one remains pinned near E_F. Self-consistent Hartree–Fock calculations reveal spontaneous flavor symmetry breaking and doping evolution of the lower band similar to that observed experimentally. However, the Hartree–Fock results do not fully explain the pinning of the upper band near E_F, suggesting that electron–electron correlation effects beyond mean-field theory are important for a full explanation.

Results

Observation of Bulk Helical Dirac Nodes and Surface Flat Bands. Fig. 1*A* shows a schematic sideview of RG. The stacking order is analogous to zigzag graphene ribbons (31) or the one-dimensional (1D) Su–Schrieffer–Heeger (SSH) topological model (32). Here, the in-plane momentum (k) kinetic term $\hbar v_F|k|$ (v_F is the Fermi velocity) and out-of-plane hopping γ_0 are mapped (up to a phase) onto the staggered hopping parameters u and w in the SSH model (33) (see *Inset* in Fig. 1*A*). In few-layer RG, each carbon sublattice hybridizes with orbitals directly above or below in the neighboring layers, forming conical subbands, while the unpaired orbitals in the outermost layers contribute to weakly dispersing surface flat bands near E_F. When increasing the layer number N, the surface flat bands become flatter and a higher density of states is expected at E_F (*SI Appendix*, Fig. S1), while the bulk bands evolve into Dirac cones. Fig. 1*B* shows the calculated electronic spectral weight for bulk RG with N = 70 layers (see *Materials and Methods* for calculation details). Here, the conical regions with light-blue colors correspond to bulk bands, whose Dirac nodes form helixes along the out-of-plane momentum (k_z) direction with opposite chiralities near the K and K′ points (28, 34, 35) (see schematic illustration in Fig. 1*C*). These bulk helical DNLs have a quantized Zak phase of π ($-\pi$) near the K (K′) point when $\hbar v_F|k| < \gamma_0$, which guarantees the existence of topologically protected "drumhead" surface states, hereafter denoted as surface topological flat bands (surface TFBs), due to the bulk-boundary correspondence (36–40). Bulk RG is therefore a model system for realizing a helical Dirac nodal line semimetal (28), where the surface TFBs (indicated by the red arrow in Fig. 1*B*) naturally arise as a result of the bulk band topology and are protected by the combined inversion- and time-reversal ($\mathcal{PT}$) symmetry.

The RG samples were prepared by mechanical exfoliation, and the ABC stacking was confirmed by spatially resolved Raman spectroscopy and NanoARPES intensity maps (*SI Appendix*, Figs. S2 and S3). Fig. 1*D* shows an overview of the characteristic

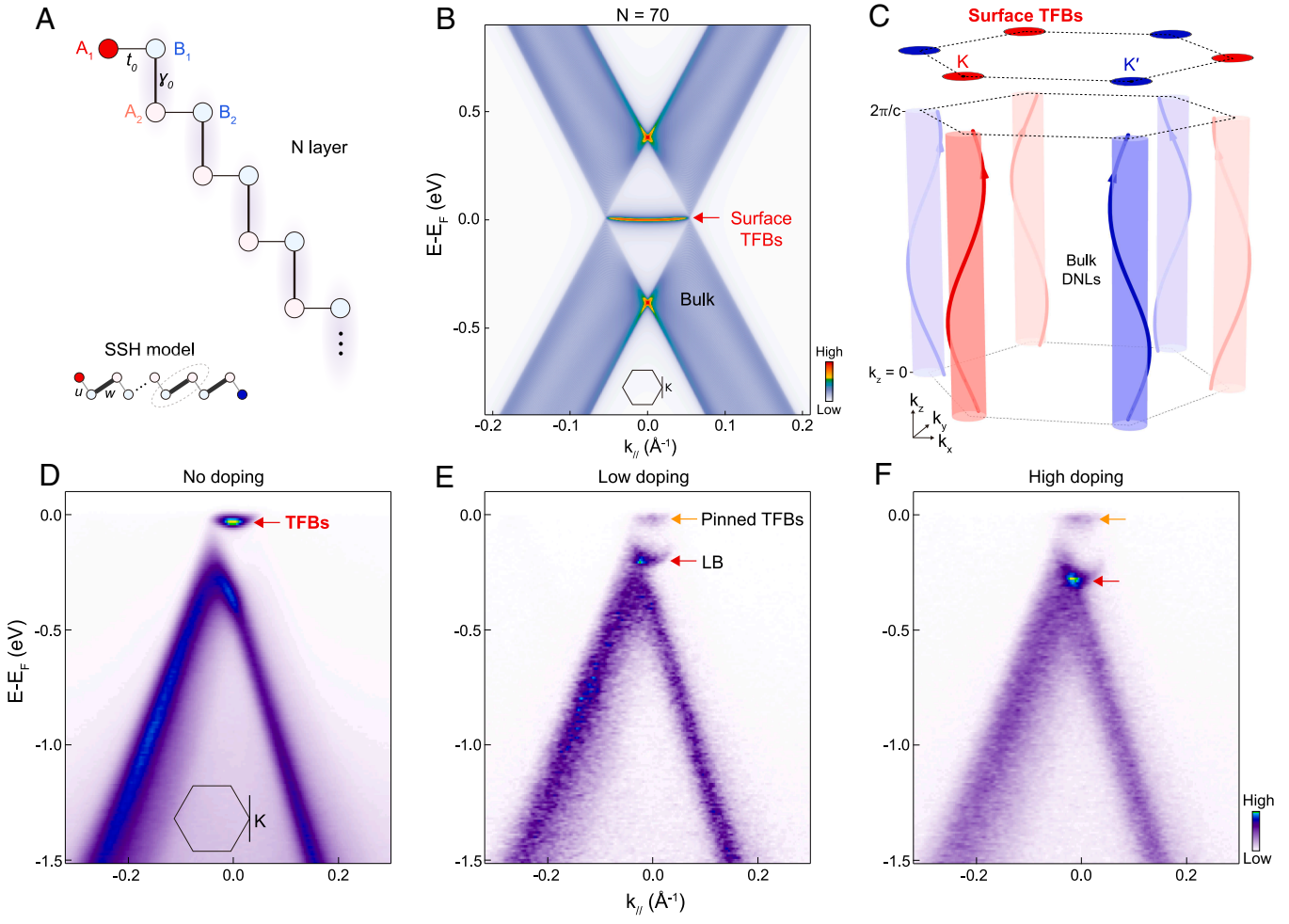

Fig. 1. Schematic illustration of RG, surface topological flat bands (surface TFBs) and bulk helical Dirac nodal lines (bulk helical DNLs), and experimental observations. (*A*) Schematic illustration of the atomic structure of bulk RG (side view), which is analogous to the SSH model (*Inset* in the *Lower Left* corner). (*B*) Calculated electronic spectral weight for RG with N = 70 layers. The surface TFBs are indicated by the red arrow, while the light-blue colors arise from the bulk conical bands. (*C*) Schematic illustration of the surface TFBs (red and blue ovals) and bulk helical DNLs (red and blue helixes). (*D*) ARPES dispersion image measured by cutting through the K point as indicated by the *Inset*. (*E* and *F*) Dispersion images measured upon low and high electron doping, respectively. The splitting of the TFBs is indicated by red and orange arrows, and the lower split band is denoted by LB.

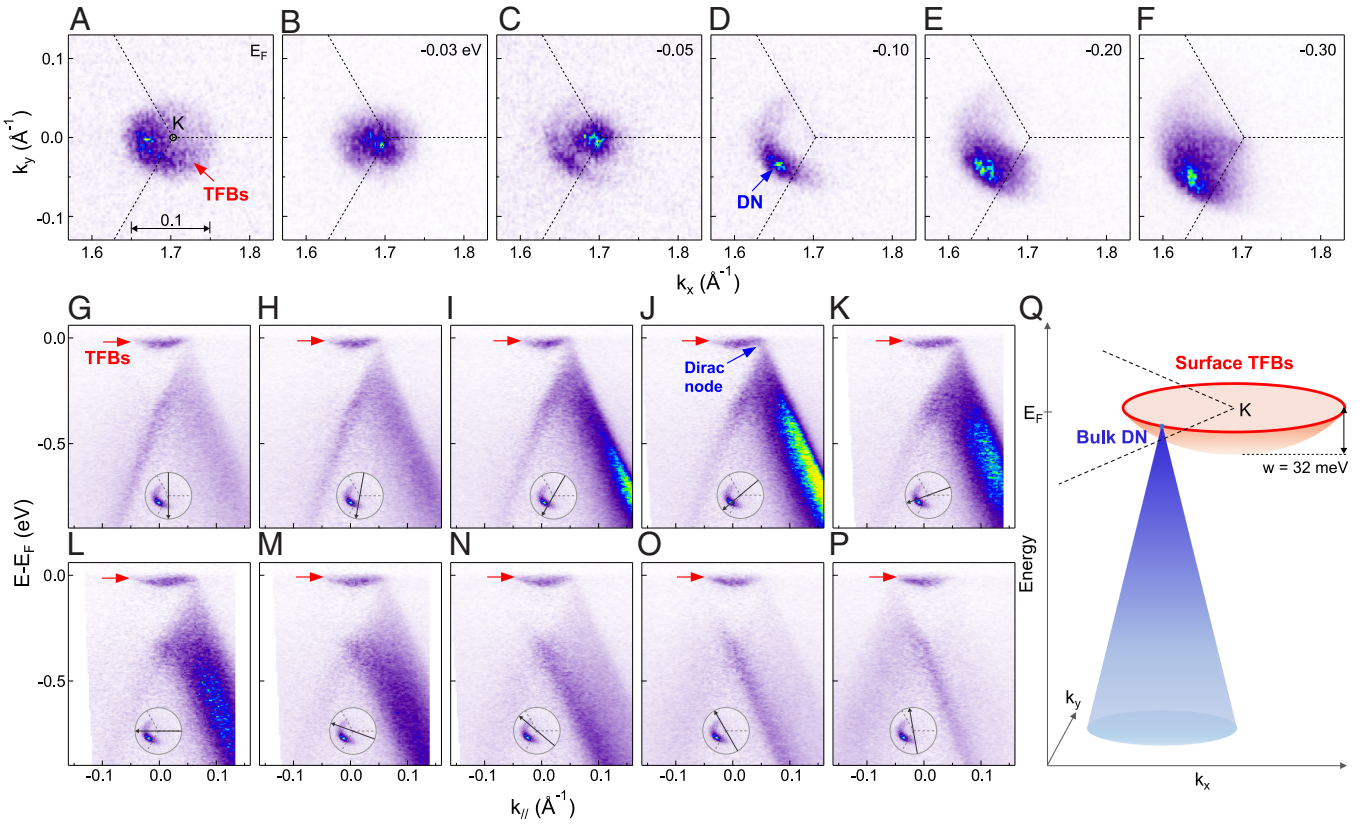

Fig. 2. Observation of surface TFBs and bulk Dirac node. (*A–F*) ARPES-measured intensity maps at a few representative energies from E_F to −0.30 eV measured on sample S2. The photon energy used is 60 eV, which corresponds to $k_z = 0.11\ c^*$ in the reduced BZ ($c^* = \frac{2\pi}{c}$, where $c = 3.34$ Å is the out-of-plane lattice constant) for the K point. The red arrow indicates the TFBs and the blue arrow in (*D*) indicates the bulk Dirac node (bulk DN). (*G–P*) Dispersion images measured by cutting through the K point along different directions indicated by arrows in the *Insets*. (*Q*) Schematic summary of the experimental electronic structure, including the DN (blue color) and the TFBs near E_F (red color).

ARPES dispersion image measured through the K point and the doping evolution. The surface TFBs near E_F (indicated by the red arrow) and the conical bulk states are clearly observed. The surface TFBs show exotic evolution upon electron doping, with a splitting of the surface TFBs indicated by orange and red arrows in Fig. 1*E*. An increase in the bandwidth is observed for the lower band at high electron doping, while the upper band is pinned near E_F (Fig. 1*F*). The origin of the surface TFBs and their correlated doping evolution are the main focus of this work.

To reveal the details of the surface TFBs and bulk states, Fig. 2 shows the experimental electronic structure of bulk RG measured at a photon energy of 60 eV. The Fermi surface map in Fig. 2*A* shows a circular-shaped pocket centered at the K point, which decreases in size and shrinks into a dot when moving down to −0.03 eV (Fig. 2*B*), indicating small bandwidth of TFBs. In addition, when moving down to −0.10 eV (Fig. 2 *C* and *D*), a bright spot is observed at the *Lower-Left* corner in Fig. 2*D* (indicated by the blue arrow), which gradually expands in size at lower energies, indicating a conical behavior (Fig. 2 *E* and *F*).

The Dirac cone and TFBs are more clearly resolved in dispersion images measured by cutting through the K point along various azimuthal angles (Fig. 2 *G–P*). The Dirac cone is most clearly observed with the sharpest dispersion when cutting through the bright spot in Fig. 2*J*, suggesting that it likely originates from the bulk band at a specific k_z value corresponding to the probe photon energy of 60 eV, while the weaker and broadened Dirac cones originate from intensity tail at other k_z values (*SI Appendix*, Fig. S4). The Dirac cone is connected to the edges of the flat band near E_F, which is observed in all cuts through the circular pockets at E_F (indicated by red arrows in Fig. 2 *G–P*). A detailed analysis of the dispersion shows that it has a bandwidth of 32 ± 7 meV and a momentum range of $\Delta k = 0.10 \pm 0.02$ Å^{-1} around the K point (see *SI Appendix*, Fig. S5 for more details). According to the theoretical models (33, 41), the momentum radius p_0 of the flat band in RG is defined by $p_0 = \gamma_0/\hbar v_F = 2\gamma_0/(\sqrt{3}at_0)$, where t_0 is the nearest-neighbor hopping and a is the lattice constant. Using the values $t_0 = 3.16$ eV, $\gamma_0 = 0.39$ eV (21), and $a = 2.46$ Å gives a momentum range of $\Delta k = 2p_0 = 0.11$ Å^{-1}, in agreement with the experimental result. Therefore, the experimental electronic structure in Fig. 2 can be summarized by the TFBs near E_F (red color) and a connecting Dirac cone (blue color), as schematically illustrated in Fig. 2*Q*.

Photon-energy-dependent ARPES measurements have been performed to further confirm that the Dirac cone originates from the three-dimensional (3D) bulk bands and the TFBs correspond to the two-dimensional (2D) surface states (see more details in *SI Appendix*, Fig. S6). Fig. 3 *A–N* shows intensity contours measured with photon energies varying from 40 eV to 105 eV, which is sufficient to cover an entire k_z Brillouin zone. The bulk Dirac node is indicated by the pink dot in Fig. 3*A*, and the intensity tail from the bottom of the TFBs is indicated by the gray dot. While the bottom of the TFBs remains fixed at the K point, the Dirac node rotates around the K point in the k_x-k_y plane when changing k_z, as indicated by the pink arrows in Fig. 3 *A–N*. The rotation period for the Dirac node agrees with the periodicity of the k_z Brillouin zone of RG (*SI Appendix*, Fig. S7).

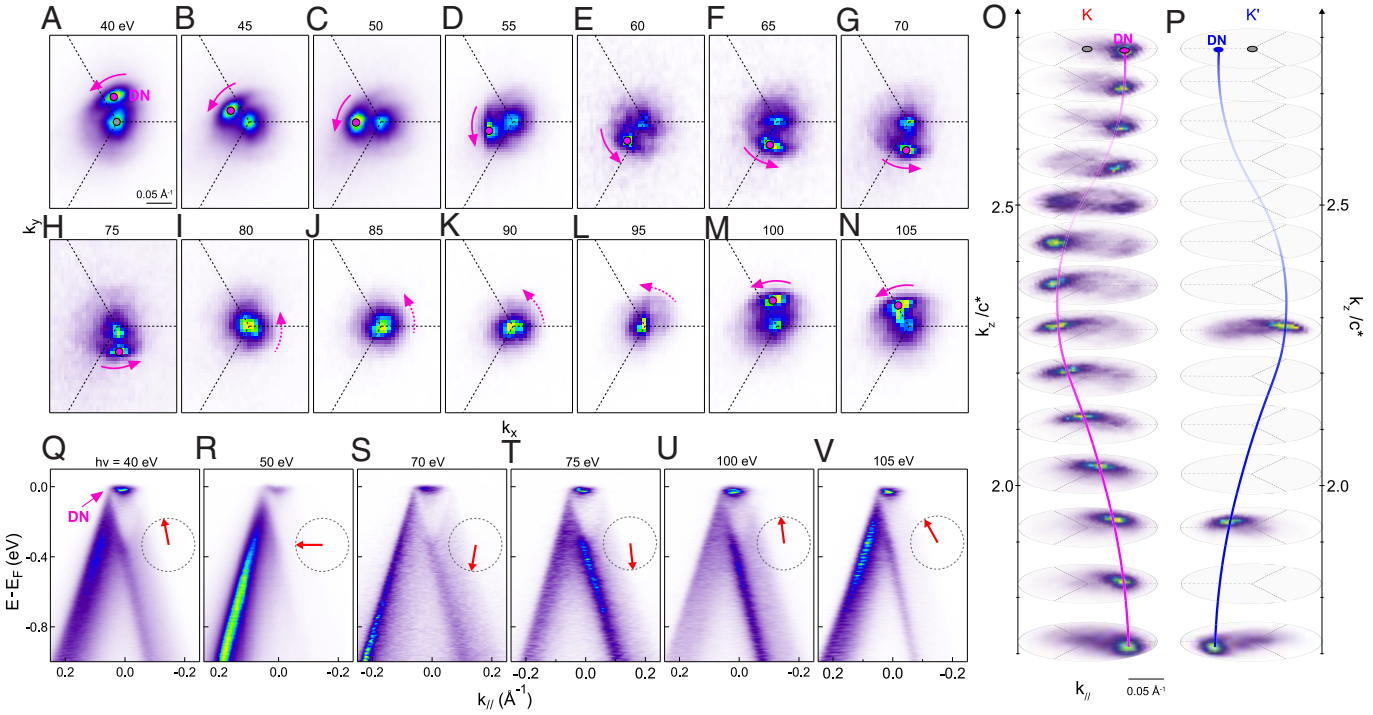

Fig. 3. Observation of bulk helical DNLs and surface TFBs along the out-of-plane momentum direction. (*A–N*) Energy contours measured at −50 meV at photon energies from 40 eV to 105 eV to show the rotation of the Dirac node as indicated by pink arrows. The Dirac node is barely detectable at 80 eV to 95 eV due to suppression of the intensity by dipole matrix element effects. (*O*) Energy contours around the K point measured at -100 meV at photon energies from 40 eV (*Bottom*) to 105 eV (*Top*), which correspond to reduced k_z values from 1.72 c^* to 2.79 c^*. (*P*) Schematic drawing of helical DNL around the K′ point, which exhibits the opposite chirality to that in the K point. (*Q–V*) Dispersion images measured at photon energies from 40 eV to 105 eV to reveal the nondispersive TFBs indicated by red arrows. All dispersion images were measured by cutting through the Dirac node and K point at each photon energy, as indicated in the *Insets*.

Fig. 3*O* shows the energy contours in the k_x-k_y-k_z space, where the helix of the Dirac nodes in 3D is indicated by the pink curve. Moreover, ARPES intensity maps covering both K and K′ valleys further show that the Dirac node helix around the K′ point has the opposite chirality to that at the K point, as schematically illustrated by the blue curve in Fig. 3*P* (see *SI Appendix*, Figs. S8 and S9 for supporting experimental data and calculations at both K and K′ valleys). Interestingly, in contrast to the k_z dependent bulk Dirac helixes which rotate with k_z, the TFBs near E_F are observed clearly at all photon energies (as indicated by red arrows in Fig. 3 *Q–V*) without noticeable k_z dependence, confirming their 2D surface state origin.

The observation of surface TFBs and bulk helical DNLs demonstrates RG to be a topological helical Dirac nodal line semimetal, where Dirac crossing points form helixes in the three-dimensional momentum space (40). Here, the TFBs form "drumhead" surface states, which are topologically protected by the bulk states. Moreover, the number of Dirac helixes is two, which is the minimum allowed by $\mathcal{PT}$ symmetry, and there are no additional bands near E_F to complicate the electronic structure. Therefore, RG provides an ideal system for investigating the physics of helical Dirac nodal line semimetals with surface TFBs as well as electron–electron correlation.

Exotic Evolution of the Surface Topological Flat Bands upon In Situ Electron Doping. The compression of electrons into the surface TFBs within a small energy range suggests enhanced electron–electron correlation. Below, we further investigate the effect of electron correlation upon in situ surface electron doping. Fig. 4 *A–J* shows a comparison of ARPES data measured at various momentum cuts on undoped (Fig. 4 *A–E*) and slightly electron-doped (Fig. 4 *F–J*) bulk RG. A splitting of the surface TFBs is clearly resolved upon electron doping (indicated by red and orange arrows in Fig. 4 *G–J*). Since the ARPES probing depth of a few Angstrom is much smaller than the sample thickness of bulk RG, one cannot detect the surface TFBs from the bottom surface. We therefore conclude that the splitting is not caused by the lifted degeneracy between the top and bottom layers, but rather by other flavors, e.g., spin or valley spontaneous symmetry breaking, or correlation-driven spectral weight splitting. Interestingly, while the upper band remains flat and pinned near E_F, the lower band becomes parabolic with an increase in the bandwidth (Fig. 4 *L–O*). At the highest doping shown in Fig. 4*O*, the energy separation between the bottoms of the upper and lower bands reaches a maximum value of approximately 400 meV. Such a drastic increase in the bandwidth by nearly one order-of-magnitude as compared to the undoped case (schematically summarized in Fig. 4 *P–R*) is an experimental signature of strong Coulomb repulsion when filling the TFBs.

Hartree–Fock Calculations Suggest Correlation Effect Beyond the mean-field theory. In order to theoretically understand the doping evolution of the surface TFBs, we perform a self-consistent Hartree–Fock (HF) calculation (see *SI Appendix* for more details). We use a semi-infinite model of RG with a top layer and infinitely many layers below. The screened Coulomb interaction is projected into the four surface TFBs corresponding to the four spin-valley flavors, within the TFBs in-plane momentum radius p_0. The interaction between two electrons separated by a distance r takes the Thomas-Fermi form $V(r) = \frac{q_e^2}{4\pi\epsilon_0 r} e^{-q_0 r}$, where we set $q_0 = 0.1$ Å^{-1}, q_e is

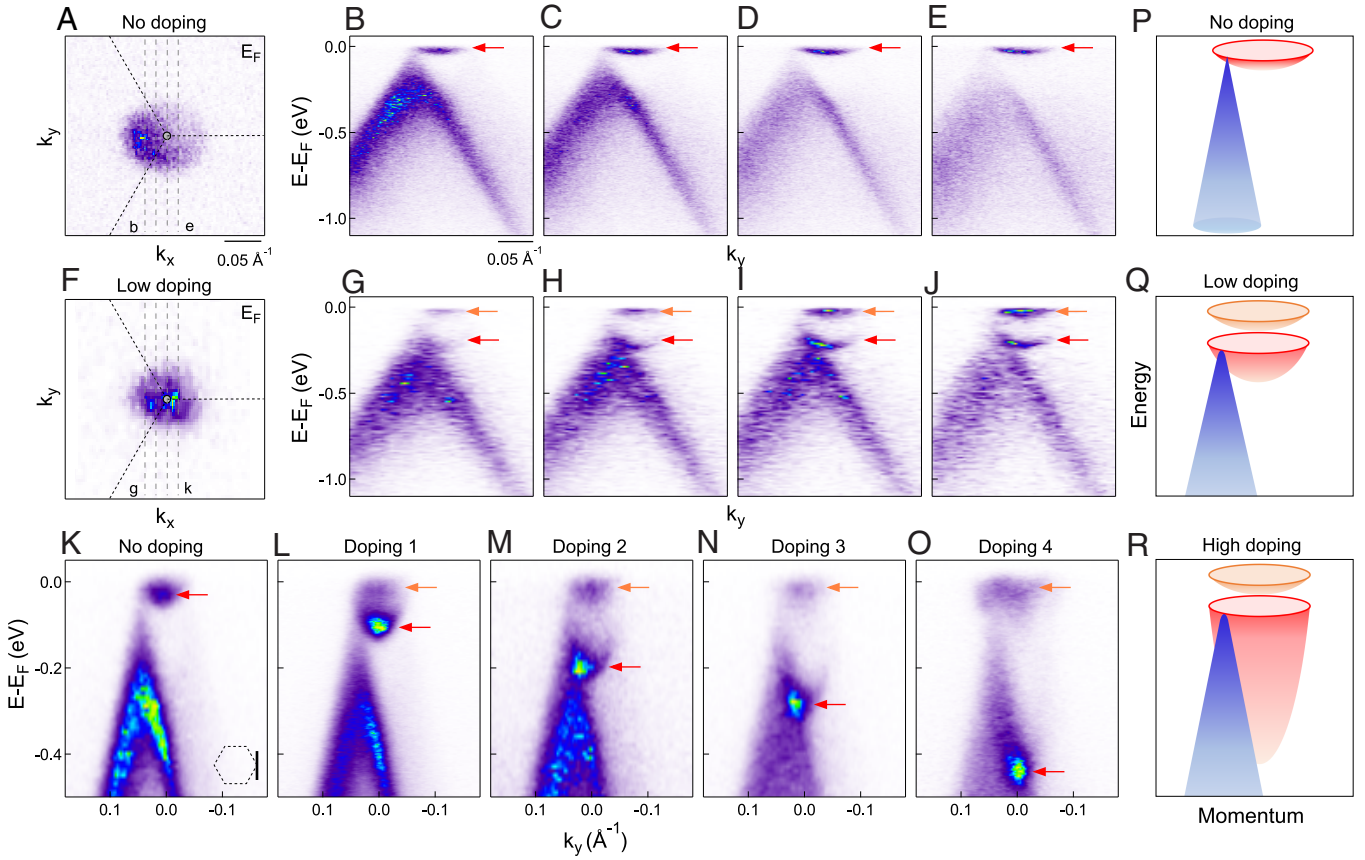

Fig. 4. Correlated evolution of the surface TFBs electronic structure upon in situ electron doping. (*A*) Fermi surface map measured before electron doping. (*B–E*) ARPES dispersion images cutting along the k_y direction as indicated by gray broken lines in (*A*). (*F*) Fermi surface map measured at low electron doping. (*G–J*) ARPES dispersion images cutting along the k_y direction as indicated by gray broken lines in (*F*). (*K–O*) ARPES Dispersion images cutting through the K point along k_y direction upon electron doping. (*P–R*) Schematics for the undoped electronic structure, flavor splitting of TFBs, and an increase in bandwidth of the lower band upon electron doping, where orange and red colors indicate the *Upper* and *Lower* split TFBs respectively. The measurements here were performed on sample S1.

the electron charge, and ϵ_0 is the vacuum permittivity. The filling factor ν refers to the top surface TFBs confined within a momentum space (with a diameter of 0.1 $Å^{-1}$) near the graphene Brillouin zone corner, which are the only states considered in the Hartree–Fock calculation (see more Hartree–Fock calculation details in *SI Appendix*). The band filling ν is defined to range from $\nu = -2$ (all surface TFBs empty) to $\nu = 2$ (all surface TFBs occupied), with the TFB defined as the drumhead TFB within the momentum radius p_0. Fig. 5 shows the evolution of the HF bands for fillings $-1.95 \leq \nu \leq -1.15$, while results for larger fillings can be found in *SI Appendix*, Fig. S10. At generic partial fillings, we observe band splitting due to the spontaneous symmetry breaking of the fourfold spin-valley degeneracy. Moreover, the bands become significantly dispersive due to the Coulomb interaction, with the energy difference between the band bottom and the Fermi level rising to the order of 400 meV, in agreement with the experimentally observed energy scale. We find that while the HF ground state is spin-valley polarized at all fillings, there are intervalley coherent states with very small excitation energy (approximately 10^{-3} or 10^{-2} meV per graphene unit cell). Therefore, the actual valley polarization may depend on factors not considered here, which is similar to what has been found in twisted bilayer graphene (TBG)(42).

Based on the comparison between HF calculation results (Fig. 5 *A–D*) with experimental results (Fig. 4 *K–O*) upon electron doping, we conjecture that the undoped RG in Fig. 4*K* is at a filling near $\nu = -2$ so that the only filled surface states are near the Fermi level with a narrow bandwidth. The experimentally observed slight filling of TFBs in the undoped graphite (Fig. 4*K*) could arise from a nonzero out-of-plane displacement field or possible doping from the substrate. As the surface electron doping increases, the lowest surface band shifts downward and curves below the Fermi level (Fig. 5 *B–D*), which may account for the lower band observed in Fig. 4 *K–O*. However, our HF calculations cannot describe the upper band pinned near the Fermi level E_F, which is observed in Fig. 4 *K–O*. We speculate that this pinned band originates from other factors such as correlation effects beyond the mean-field theory. For example, the surface flat bands and bulk dispersive bands here may resemble the topological Kondo model of TBG (43) consisting of flat bands and dispersive bands, which results in a Kondo resonance spectral weight peak at the Fermi level (44–47), as observed experimentally in TBG (48). Further theoretical investigations are needed to establish a full understanding regarding the pinning of flat band upon doping.

Conclusion and Outlook. The finding of topologically protected surface TFBs makes bulk RG a unique platform for bridging intriguing physics in various dimensionalities, such as the edge state of 1D zigzag graphene ribbons (31, 49), 2D flat bands in moiré superlattices (50), and 3D nodal line semimetals with the 3D quantum Hall effect (51). The coexistence of nontrivial topological physics and correlation effects provides opportunities for exploring intertwined topological physics and

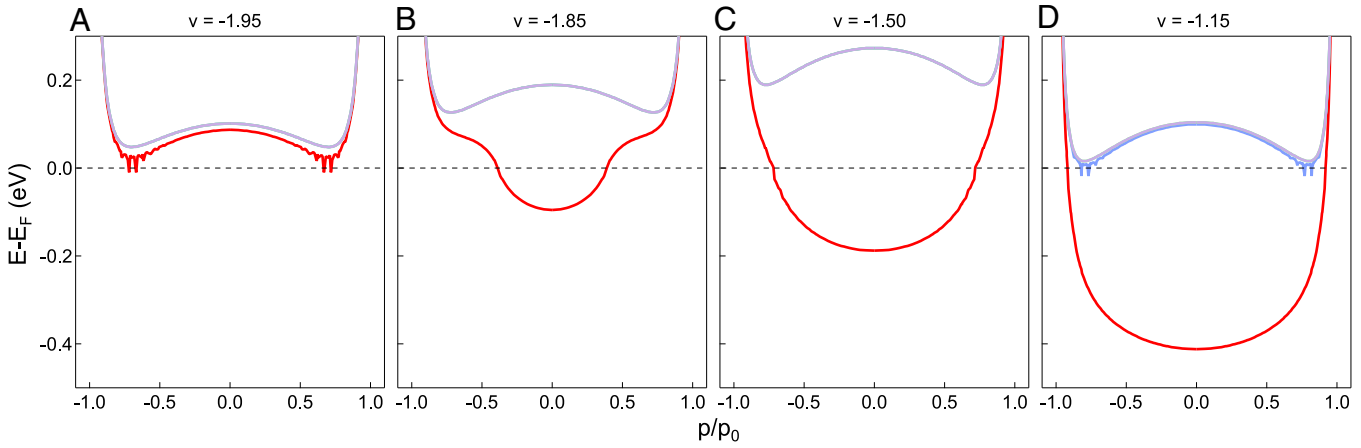

Fig. 5. Hartree–Fock band structures at negative fillings. (*A*–*D*) Self-consistent Hartree–Fock calculations of the surface TFBs at fillings of $\nu = -1.95$, -1.85, -1.50, and -1.15, respectively. Each panel shows the four resulting Hartree–Fock bands. The *Top* three bands are degenerate. The *Bottom* of the lowest TFB (red curve) moves from near the Fermi level to approximately -400 meV (see *SI Appendix*, Fig. S10 for similar plots at fillings of $\nu = -1.0$, -0.8, -0.4, and 0.0).

interaction-driven competing symmetry-broken states, such as high-temperature surface superconductivity (29), topological superconductivity, and chiral superconductivity (30).

Materials and Methods

Sample Preparation. The bulk RG samples were prepared using a clean dry transfer method. First, graphite flakes were exfoliated by Polydimethylsiloxane (PDMS), and the stacking of RG was identified by Raman spectroscopy measurements (*SI Appendix*, Fig. S2). Second, the RG flakes were transferred onto substrates such as a gold-coated substrate (sample S1, sample S3, and sample S5), a *p*-type Si substrate (sample S2), or BN/Au/SiO_2//Si (sample S4) to ensure good electrical conductivity for ARPES measurements. Before ARPES measurements, the RG stacking was further confirmed by spatially resolved Raman spectroscopy to verify that the stacking order did not change during the transfer process (*SI Appendix*, Fig. S3). By combining optical images, Raman spectroscopy, NanoARPES, and Atomic-force microscope measurements, we are able to identify RG regions and obtain the intrinsic electronic structure from RG.

ARPES Measurement. MicroARPES and NanoARPES measurements were performed at a vacuum better than 2×10^{-10} torr at beamline 4.0.3 of the Advanced Light Source at Lawrence Berkeley National Laboratory (LBNL), Analysis Nano-spoT Angle Resolved photoEmission Spectroscopy (ANTARES) of the Synchrotron Source Optimisée de Lumière à Energie Intermédiaire du LURE (SOLEIL) in France, and BL03U of the Shanghai Synchrotron Radiation Facility (SSRF), with beam sizes of 30 μm, 500 nm to 700 nm, and 15 μm to 20 μm, respectively. Before ARPES measurements, the RG samples were annealed at 200 °C in ultrahigh vacuum until sharp dispersions were observed. The surface electron doping was achieved by in situ deposition of Rb through heating an SAES commercial dispenser in situ.

Data, Materials, and Software Availability. All study data are included in the article and/or *SI Appendix*.

ACKNOWLEDGMENTS. We acknowledge useful discussions with Haizhou Lu, Jing Wang, and Yves H. Kwan. This work is supported by the National Key R&D Program of China (Grant Number 2021YFA1400100), the National Natural Science Foundation of China (Grant Numbers 12234011, 12421004, 52388201, 52025024, 92250305, 12327805, and 11725418). H.Z. and C.B. acknowledge support from the Shuimu Tsinghua Scholar program, the Project funded by China Postdoctoral Science Foundation (Grant Numbers 2022M721887 and 2022M721886), and the National Natural Science Foundation of China (Grant Number 12304226). M.G.S. and B.L. acknowledge support from NSF through Princeton University's Materials Research Science and Engineering Center DMR-2011750, and the NSF under award DMR-2141966. K.W. and T.T. acknowledge support from the Japan Society for the Promotion of Science KAKENHI Grant-in-Aid for Scientific Research (Grant Numbers 20H00354 and 23H02052) and World Premier International Research Center Initiative, Ministry of Education, Culture, Sports, Science and Technology, Japan. This research used resources of the Advanced Light Source, which is a Department of Energy Office of Science User Facility under contract Number DE-AC02-05CH11231. Part of this research also used the Beamline 03U of the Shanghai Synchrotron Radiation Facility, which is supported by SiP·ME^2 project under Contract Number 11227902 from National Natural Science Foundation of China. We acknowledge SOLEIL for the provision of synchrotron radiation facilities of beamline ANTARES.

Author affiliations: [a]State Key Laboratory of Low-Dimensional Quantum Physics and Department of Physics, Tsinghua University, Beijing 100084, People's Republic of China; [b]Department of Physics, Princeton University, Princeton, NJ 08544; [c]Institute for Advanced Study, Tsinghua University, Beijing 100084, People's Republic of China; [d]Research Center for Functional Materials, National Institute for Materials Science, Tsukuba 305-0044, Japan; [e]International Center for Materials Nanoarchitectonics, National Institute for Materials Science, Tsukuba 305-0044, Japan; [f]Shanghai Synchrotron Radiation Facility, Shanghai Advanced Research Institute, Chinese Academy of Sciences, Shanghai 201210, People's Republic of China; [g]School of Materials Science and Engineering, Beihang University, Beijing 100191, People's Republic of China; [h]Max Planck Institute for the Structure and Dynamics of Matter, Center for Free Electron Laser Science, Hamburg 22761, Germany; [i]Frontier Science Center for Quantum Information, Beijing 100084, People's Republic of China; [j]Synchrotron SOLEIL, L'Orme des Merisiers, Gif sur Yvette Cedex 91192, France; and [k]Advanced Light Source, Lawrence Berkeley National Laboratory, Berkeley, CA 94720

1. Y. Cao *et al.*, Unconventional superconductivity in magic-angle graphene superlattices. *Nature* **556**, 43–50 (2018).
2. Y. Cao *et al.*, Correlated insulator behaviour at half-filling in magic-angle graphene superlattices. *Nature* **556**, 80–84 (2018).
3. M. Serlin *et al.*, Intrinsic quantized anomalous Hall effect in a moiré heterostructure. *Science* **367**, 900–903 (2020).
4. T. Han *et al.*, Large quantum anomalous Hall effect in spin-orbit proximitized rhombohedral graphene. *Science* **384**, 647–651 (2024).
5. Z. Lu *et al.*, Fractional quantum anomalous Hall effect in a graphene moiré superlattice. *Nature* **626**, 759–764 (2024).
6. M. F. Craciun *et al.*, Trilayer graphene is a semimetal with a gate-tunable band overlap. *Nat. Nanotechnol.* **4**, 383–388 (2009).
7. C. H. Lui, Z. Li, K. F. Mak, E. Cappelluti, T. F. Heinz, Observation of an electrically tunable band gap in trilayer graphene. *Nat. Phys.* **7**, 944–947 (2011).
8. W. Bao *et al.*, Stacking-dependent band gap and quantum transport in trilayer graphene. *Nat. Phys.* **7**, 948–952 (2011).
9. G. Chen *et al.*, Evidence of a gate-tunable Mott insulator in a trilayer graphene moiré superlattice. *Nat. Phys.* **15**, 237–241 (2019).
10. G. Chen *et al.*, Signatures of tunable superconductivity in a trilayer graphene moiré superlattice. *Nature* **572**, 215–219 (2019).
11. G. Chen *et al.*, Tunable correlated Chern insulator and ferromagnetism in a moiré superlattice. *Nature* **579**, 56–61 (2019).
12. H. Zhou, T. Xie, T. Taniguchi, K. Watanabe, A. F. Young, Superconductivity in rhombohedral trilayer graphene. *Nature* **598**, 434–438 (2021).

13. H. Zhou *et al*., Half- and quarter-metals in rhombohedral trilayer graphene. *Nature* **598**, 429–433 (2021).
14. J. Yang *et al*., Spectroscopy signatures of electron correlations in a trilayer graphene/hBN moiré superlattice. *Science* **375**, 1295–1299 (2022).
15. A. Kerelsky *et al*., Moiréless correlations in ABCA graphene. *Proc. Natl. Acad. Sci. U.S.A.* **118**, e2017366118 (2021).
16. K. Liu *et al*., Spontaneous broken-symmetry insulator and metals in tetralayer rhombohedral graphene. *Nat. Nanotechnol.* **19**, 188–195 (2024).
17. Y. Sha *et al*., Observation of a Chern insulator in crystalline ABCA-tetralayer graphene with spin-orbit coupling. *Science* **384**, 414–419 (2024).
18. Y. Shi *et al*., Electronic phase separation in multilayer rhombohedral graphite. *Nature* **584**, 210–214 (2020).
19. T. Han *et al*., Correlated insulator and Chern insulators in pentalayer rhombohedral-stacked graphene. *Nat. Nanotechnol.* **19**, 181–187 (2024).
20. T. Han *et al*., Orbital multiferroicity in pentalayer rhombohedral graphene. *Nature* **623**, 41–47 (2023).
21. M. Koshino, E. McCann, Trigonal warping and Berry's phase Nπ in ABC-stacked multilayer graphene. *Phys. Rev. B* **80**, 165409 (2009).
22. F. Zhang, B. Sahu, H. Min, A. H. MacDonald, Band structure of ABC-stacked graphene trilayers. *Phys. Rev. B* **82**, 035409 (2010).
23. C. Coletti *et al*., Revealing the electronic band structure of trilayer graphene on SiC: An angle-resolved photoemission study. *Phys. Rev. B* **88**, 155439 (2013).
24. D. Pierucci *et al*., Evidence for flat bands near the Fermi level in epitaxial rhombohedral multilayer graphene. *ACS Nano* **9**, 5432–5439 (2015).
25. C. Bao *et al*., Stacking-dependent electronic structure of trilayer graphene resolved by nanospot angle-resolved photoemission spectroscopy. *Nano Lett.* **17**, 1564–1568 (2017).
26. W. Wang *et al*., Flat-band electronic structure and interlayer spacing influence in rhombohedral four-layer graphene. *Nano Lett.* **18**, 5862–5866 (2018).
27. H. Henck *et al*., Flat electronic bands in long sequences of rhombohedral-stacked graphene. *Phys. Rev. B* **97**, 245421 (2018).
28. T. T. Heikkilä, G. E. Volovik, Dimensional crossover in topological matter: Evolution of the multiple Dirac point in the layered system to the flat band on the surface. *JETP Lett.* **93**, 59–65 (2011).
29. N. B. Kopnin, T. T. Heikkilä, G. E. Volovik, High-temperature surface superconductivity in topological flat-band systems. *Phys. Rev. B* **83**, 220503 (2011).
30. A. Ghazaryan, T. Holder, E. Berg, M. Serbyn, Multilayer graphenes as a platform for interaction-driven physics and topological superconductivity. *Phys. Rev. B* **107**, 104502 (2023).
31. Y. W. Son, M. L. Cohen, S. G. Louie, Half-metallic graphene nanoribbons. *Nature* **444**, 347–349 (2006).
32. W. P. Su, J. R. Schrieffer, A. J. Heeger, Solitons in polyacetylene. *Phys. Rev. Lett.* **42**, 1698–1701 (1979).
33. R. Xiao *et al*., Density functional investigation of rhombohedral stacks of graphene: Topological surface states, nonlinear dielectric response, and bulk limit. *Phys. Rev. B* **84**, 165404 (2011).
34. J. McClure, Electron energy band structure and electronic properties of rhombohedral graphite. *Carbon* **7**, 425–432 (1969).
35. C. H. Ho, C. P. Chang, M. F. Lin, Evolution and dimensional crossover from the bulk subbands in ABC-stacked graphene to a three-dimensional Dirac cone structure in rhombohedral graphite. *Phys. Rev. B* **93**, 075437 (2016).
36. A. A. Burkov, M. D. Hook, L. Balents, Topological nodal semimetals. *Phys. Rev. B* **84**, 235126 (2011).
37. C. Fang, Y. Chen, H. Y. Kee, L. Fu, Topological nodal line semimetals with and without spin-orbital coupling. *Phys. Rev. B* **92**, 081201 (2015).
38. Y. Kim, B. J. Wieder, C. L. Kane, A. M. Rappe, Dirac line nodes in inversion-symmetric crystals. *Phys. Rev. Lett.* **115**, 036806 (2015).
39. H. Weng *et al*., Topological node-line semimetal in three-dimensional graphene networks. *Phys. Rev. B* **92**, 045108 (2015).
40. C. Fang, H. Weng, X. Dai, Z. Fang, Topological nodal line semimetals. *Chin. Phys. B* **25**, 117106 (2016).
41. T. Hyart, R. Ojajärvi, T. T. Heikkilä, Two topologically distinct Dirac-line semimetal phases and topological phase transitions in rhombohedrally stacked honeycomb lattices. *J. Low Temp. Phys.* **191**, 35–48 (2018).
42. K. P. Nuckolls *et al*., Quantum textures of the many-body wavefunctions in magic-angle graphene. *Nature* **620**, 525–532 (2023).
43. Z. D. Song, B. A. Bernevig, Magic-angle twisted bilayer graphene as a topological heavy Fermion problem. *Phys. Rev. Lett.* **129**, 047601 (2022).
44. H. Shi, X. Dai, Heavy-fermion representation for twisted bilayer graphene systems. *Phys. Rev. B* **106**, 245129 (2022).
45. Y. Z. Chou, S. Das Sarma, Kondo lattice model in magic-angle twisted bilayer graphene. *Phys. Rev. Lett.* **131**, 026501 (2023).
46. H. Hu *et al*., Symmetric Kondo lattice states in doped strained twisted bilayer graphene. *Phys. Rev. Lett.* **131**, 166501 (2023).
47. G. D. Zhou, Y. J. Wang, N. Tong, Z. D. Song, Kondo phase in twisted bilayer graphene. *Phys. Rev. B* **109**, 045419 (2024).
48. D. Wong *et al*., Cascade of electronic transitions in magic-angle twisted bilayer graphene. *Nature* **582**, 198–202 (2020).
49. G. Z. Magda *et al*., Room-temperature magnetic order on zigzag edges of narrow graphene nanoribbons. *Nature* **514**, 608–611 (2014).
50. P. A. Pantaleón *et al*., Superconductivity and correlated phases in non-twisted bilayer and trilayer graphene. *Nat. Rev. Phys.* **5**, 304–315 (2023).
51. C. H. Ho, C. P. Chang, M. F. Lin, Landau subband wave functions and chirality manifestation in rhombohedral graphite. *Solid State Commun.* **197**, 11–15 (2014).